

Subpixel Melt Index In Antarctic Peninsula Using Spatially Constrained Linear Unmixing From Time Series Satellite Passive Microwave Images

Lei Wang¹ and Dan Tian¹

¹Louisiana State University

November 24, 2022

Abstract

The inevitable coarse pixels (~ 25 km) of satellite passive microwave images introduced large uncertainty to the surface melt area estimation on Antarctic ice margins. Our test showed that the melt index of the Austral year 2012-13 in the Antarctic Peninsula calculated from the high resolution product was 33% lower than the original Special Sensor Microwave/Imager (SSM/I) images. Therefore, by allowing for fractional melt estimation, a subpixel mapping method was adopted in this research to improve the accuracy and reliability of surface melt measurement from passive microwave images. This innovative method uses the least squares mixture analysis (LSMA) on the time series of daily passive microwave images by taking advantage of their high temporal resolution. The endmembers for the unmixing calculation were collected under the constraint of voronoi polygons. The fractional melt index of each pixel was calculated by multiplying its area with melt fraction. By using the high resolution passive microwave earth system data record (PMESDR) dataset as the reference, we found that compared with the original SSM/I images, the overestimation of surface melt was corrected by the unmixing analysis. A log-linear regression between melt fraction and elevation showed that the melt fraction is inversely correlated to the elevation, and the topography is the dominant factor for melt fraction distribution in high elevations. We recommend such a treatment of linear unmixing analysis on the passive microwave images to be used for future surface melt mapping in Antarctica and Greenland.

1 **Subpixel Melt Index In Antarctic Peninsula Using Spatially Constrained Linear**
2 **Unmixing From Time Series Satellite Passive Microwave Images**

3 **Dan Tian¹ and Lei Wang^{1*}**

4 ¹ Department of Geography & Anthropology, Louisiana State University, Baton Rouge, LA
5 70810.

6 *Corresponding author: Lei Wang (leiwang@lsu.edu) <https://orcid.org/0000-0003-1298-4839>

7 **Key Points:**

- 8 • The overestimation of the Boolean surface melt maps in the Antarctic Peninsula could be
9 as large as 56%.
- 10 • The least squares mixture analysis offers to offset the bias in the Boolean surface melt
11 maps created from satellite radiometers.
- 12 • Elevation plays an important role in the partial melting. phenomenon on Antarctic ice
13 sheets.

14 **Abstract**

15 The inevitable coarse pixels (~25 km) of satellite passive microwave images introduced large
16 uncertainty to the surface melt area estimation on Antarctic ice margins. Our test showed that the
17 melt index of the Austral year 2012-13 in the Antarctic Peninsula calculated from the high
18 resolution product was 33% lower than the original Special Sensor Microwave/Imager (SSM/I)
19 images. Therefore, by allowing for fractional melt estimation, a subpixel mapping method was
20 adopted in this research to improve the accuracy and reliability of surface melt measurement
21 from passive microwave images. This innovative method uses the least squares mixture analysis
22 (LSMA) on the time series of daily passive microwave images by taking advantage of their high
23 temporal resolution. The endmembers for the unmixing calculation were collected under the
24 constraint of voronoi polygons. The fractional melt index of each pixel was calculated by
25 multiplying its area with melt fraction. By using the high resolution passive microwave earth
26 system data record (PMESDR) dataset as the reference, we found that compared with the
27 original SSM/I images, the overestimation of surface melt was corrected by the unmixing
28 analysis. A log-linear regression between melt fraction and elevation showed that the melt
29 fraction is inversely correlated to the elevation, and the topography is the dominant factor for
30 melt fraction distribution in high elevations. We recommend such a treatment of linear unmixing
31 analysis on the passive microwave images to be used for future surface melt mapping in
32 Antarctica and Greenland.

33 **Plain Language Summary**

34 Surface melt could be one of the major causes of the recent and historical disintegration of
35 Antarctic ice shelves. Tracking and monitoring surface melt from satellites are crucial to better
36 understanding of how the regional and global climate is changing and the relationship between
37 climate change and glacier dynamics. However, none of the current satellites provides
38 sufficiently detailed data for scientists to measure surface melt with high confidence and
39 accuracy. We found that the current estimation of surface melt in the Antarctic Peninsula could
40 be 56% larger than its actual value because of the signal mixing problem. Therefore, we propose
41 a subpixel estimating method that is able to offset the overestimation problem in the previous
42 research. The new melt map was proved more accurate and reliable for interannual trend
43 analysis.

44 **1. Introduction**

45 Mapping surface melt on Antarctic Ice Shelves is of great significance for studying glacier
46 dynamics and regional and global climate changes. Melting snow has a low visible and near-
47 infrared albedo, absorbing up to four times as much solar radiation as dry snow (Steffen, 1995).
48 In addition, percolating melt water accelerates iceberg calving and causes ice mass loss and ice
49 front retreat (Holland, 2010). Antarctica Ice Shelves are sensitive to the warming temperature.
50 As shown in Zwally and Fiegles (1994), surface melt intensity is related to the locally
51 accumulative number of days above the melting temperature. Consistent and intense surface melt
52 contributed to enlarged ice crevasses (Scambos et al., 2000), accelerated glacier flow (Zwally,
53 2002), and disintegration of ice tongues (van den Broeke, 2005). Monitoring surface melt
54 phenomena is a key to understanding regional and global climate changes (Doake & Vaughan,
55 1991; Gilbert & Domack, 2003; MacAYEAL et al., 2003; Vaughan & Doake, 1996).

56 Antarctica has the highest winds, lowest temperatures, and highest average elevation on
57 Earth. Severe weather, poor accessibility, long and dark polar nights in winter, and logistical
58 difficulties give rise to serious challenges to traditional field observations. Satellite passive
59 microwave data capture surface emission from water, vegetation, soil, and snow and ice under all
60 weather conditions, and have become the only data source capable of continuously monitoring
61 surface melt in Antarctica (Liu et al., 2006) for long terms. The Defense Meteorological Satellite
62 Program (DMSP) operated by National Oceanic and Atmospheric Administration (NOAA) has
63 launched a series of satellites since 1978 with the payload of multiple generation passive
64 microwave sensors including scanning multichannel microwave radiometer (SMMR), Special
65 Sensor Microwave/Imager (SSM/I), and Special Sensor Microwave Imager Sounder (SSMIS).
66 Glacier and ice sheet surface melting was mapped from this dataset for Greenland (Abdalati &
67 Steffen, 1995, 1997, 2001; Liang et al., 2019; Mote et al., 1993; Mote & Anderson, 1995) and
68 Antarctica (Fahnestock et al., 2002; Liang et al., 2019; Liu et al., 2006; Ridley, 1993; Torinesi et
69 al., 2003; Zwally & Fiegles, 1994).

70 Large Instantaneous field of view is required for passive microwave sensors to achieve
71 sufficient signal-to-noise ratio from satellite orbits that are usually placed at 700~800 km above
72 the ground elevation. The nominal ground spacing of the SSM/I pixels obtained at the 19 GHz
73 channel, for example, is 25 km. In other words, any ground objects or processes that are smaller
74 than 25 km will not be accurately measured. Therefore, uncertainty due to the large pixel size
75 exists in the melt maps derived at the 25 km scale and could be large enough to distort our
76 knowledge of climate changes derived from the melt maps. Consistent decreasing trends of
77 surface melt over the Antarctic continent were reported by different research groups using the
78 satellite passive microwave data (Liang et al., 2019; Liu et al., 2006; Tedesco, 2009; Wang &
79 Liu, 2017). These reported trends, however, were contradictory to the warming climate records
80 in Antarctica (Steig et al., 2009) and increasing sea levels caused by ice sheet melt (Golledge et
81 al., 2019). The uncertainty of surface melt records from the passive microwave data could
82 contribute to such inconsistency between the surface melt trend in Antarctica and other
83 climatological reports. The work by De Freitas et al. (2018) suggested that the Boolean
84 classification of melt and non-melt status of the large SSM/I pixels would overestimate melt
85 extents. They proposed an unmixing method using four channels (19H, 19V, 37H, and 37V) of

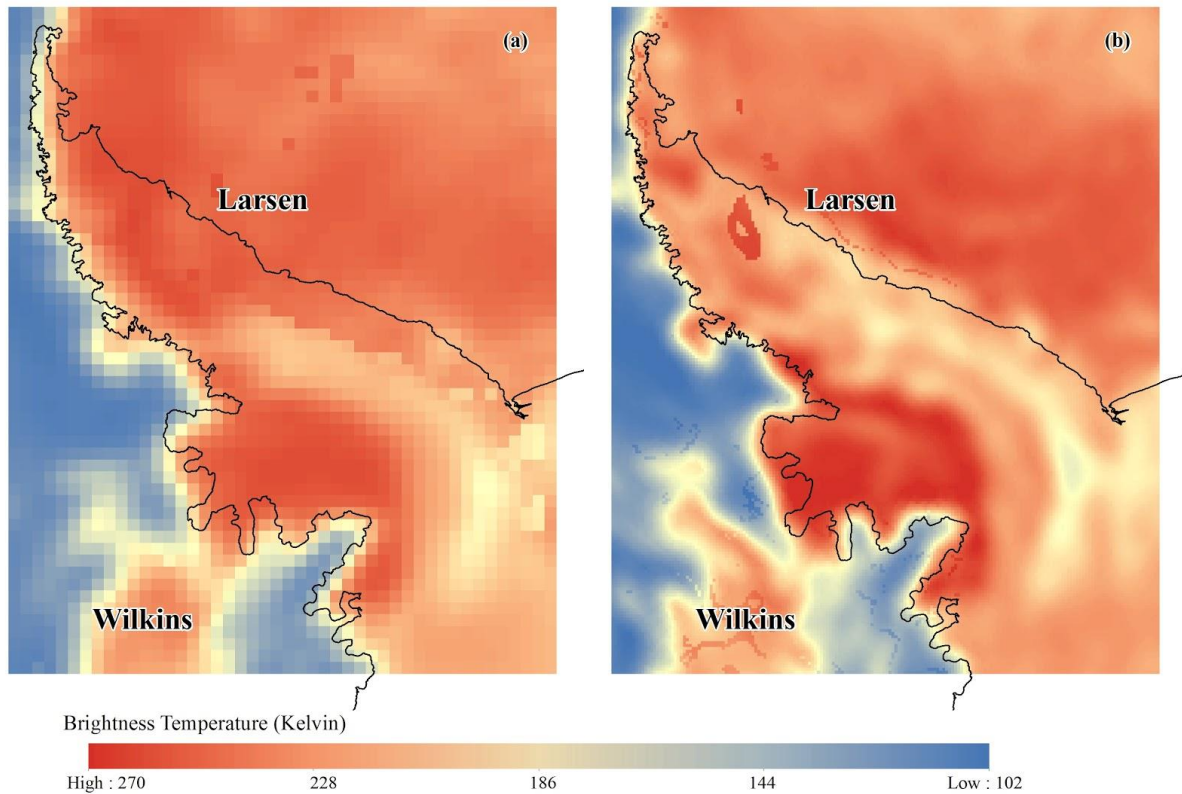


Figure 1: Study area of the Antarctic Peninsula. (a) The SSM/I image and (b) the PMESDR image of December 31, 2012

86 SSM/I to unmix three endmembers: wet snow, dry snow, and rock outcrops. Their method,
 87 however, is limited by the number of channels and cannot unmix more than three endmembers.
 88 And the high similarity among the four channels in their responses to melting and non-melting
 89 status compromises the unmixing model premise. The brightness temperature of dry snow can
 90 range from 175 K to 235 K because of the large variation of the emissivity, which is strongly
 91 dependent on the grain-size (Zwally & Fiegles, 1994). Therefore, it is difficult to determine pure
 92 dry endmembers only based on the absolute brightness temperature. In this research, we propose
 93 a new unmixing algorithm that (1) treats the time series brightness temperature data as
 94 hyperspectral images and (2) identifies endmembers by searching distances. The objective of this
 95 paper is twofold: (1) to quantify the overestimation bias of the existing SSM/I surface melt maps
 96 and (2) to verify that our new unmixing method can reduce the uncertainty and correct the bias
 97 of melt map production from passive microwave remote sensing data.

98 2. Data and study area

99 Figure 1 shows the boundary and coastline of the study area overlaid with the SSM/I image (a)
 100 and the PMESDR image (b) of December 31, 2012. The study area is measured as 1,150 km by

1,400 km, with 584,375 km² of land surface area. The passive microwave images were obtained by the Special Sensor Microwave/Imager (SSM/I) onboard the Defense Meteorological Satellite Program (DMSP) satellites, which measures microwave brightness temperature of the atmosphere, ocean, and terrain (NOAA, 2019). It offers daily data since 1987 in vertical polarization 22.235 GHz and both horizontal and vertical polarization 19.35, 37.0, and 85.5 GHz (Armstrong et al., 1994). Among the 7 channels, Liu et al. (2006) made a comparison of the brightness temperature of different frequencies and polarizations and found that the low frequency channels were more sensitive to melt initiation than the channels at higher frequencies. This is mainly because both absorption and emission of microwave radiation are stronger at higher frequency. About polarization, according to Abdalati and Steffen (1997) and Liu et al. (2006), at the same frequency, the conversion from dry snow to wet snow leads to a greater increase in the brightness temperature of horizontal polarization than that of vertical polarization. Based on these findings, the brightness temperature data at the satellite ascending nodes from July 1, 2012 to June 30, 2013 at the 19 GHz frequency with the horizontal polarization were chosen for this study.

For validation of the subpixel fraction derived from the unmixing algorithm, we used the enhanced resolution passive microwave earth system data record (PMESDR) produced from the MEaSUREs program funded by NASA, which used the proven interpolation method (David G. Long & Brodzik, 2016; D. G. Long & Daum, 1998) to reprocess and fuse the complete data records of SMMR, SSM/I-SSMIS and AMSR-E in a single grid passive microwave ESDR with improved resolution. The interpolation algorithm takes advantage of overlapping and oversampling satellite IFOVs to reconstruct the high resolution image (Brodzik & Long, 2015). The dataset we used was the calibrated enhanced resolution passive microwave daily grid 2.0 brightness temperature ESDR, version 1 (CETB) ESDR using the latest improved level 2 SSM/I-SSMIS and AMSR-E data recording (Brodzik et al., 2018). For channel 19H, the best resolution achieved by the interpolation is 6.25 km, which is set by the 25-km base resolution and power-of-2 dividers. Therefore, each original SSM/I pixel is nested by 16 PMESDR pixels. We use the melt fraction derived from each set of 16 PMESDR pixels to verify the melt fraction calculated from the least squares mixture analysis described below.

3. Methods

3.1. Melt detection

On ice sheets and ice shelves, passive microwave sensors detect naturally emitted microwave energy from both dry and melting snows within their field of view. Measured passive microwave data is in the form of brightness temperature calibrated based on the recorded microwave energy. The relationship between the calculus brightness temperature (T_b) and the near-surface physical temperature (T_s) can be expressed by first-order Rayleigh-Jeans approximation (Zwally & Gloersen, 1977) in the microwave spectra:

$$T_b = \varepsilon \cdot T_s \quad (1)$$

where ε is the emissivity of snow near the surface. The emissivity of wet snow in the microwave region is about 0.9, while that of dry snow varies from 0.65 to 0.85, which is depending on the

141 particle size, because the scattering by ice grains of the radiation emitting from deeper layers in
 142 snow packs will reduce the emissivity. Therefore, assuming the temperature at the melting point
 143 of ice (273.6 K), the theoretical brightness temperature of wet snows is 246 K, which is about 15
 144 to 70 degrees above the brightness temperature of dry snows (Zwally & Fiegles, 1994). When
 145 dry snow packs start to melt, the brightness temperature will rise drastically even if the physical
 146 temperature does not change. Similarly, brightness temperature will drop back to the premelting
 147 status when the snow packs refreeze. Microwave sensors with a frequency higher than 10 GHz
 148 can detect the increase and decrease of brightness temperature when snow begins to melt and
 149 refreezes, respectively (Liu et al., 2006). Such brightness temperature changes, rather than
 150 physical temperature fluctuations, can be used to track the melt and refreeze events during an
 151 austral summer from satellite observations.

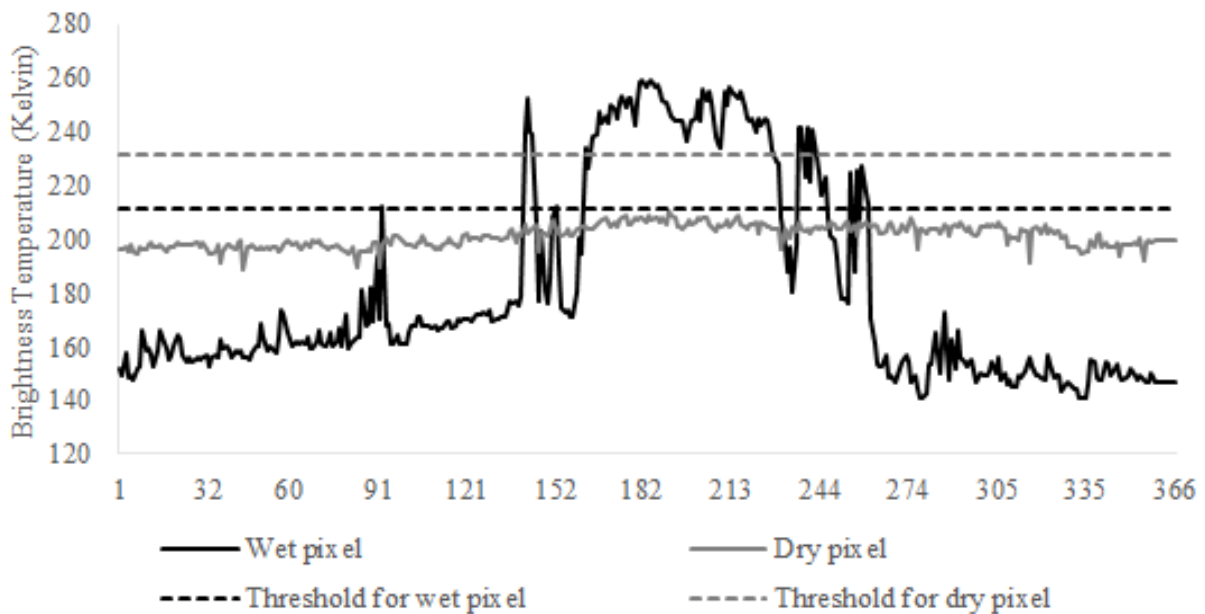


Figure 2: The annual variations of brightness temperature for typical wet and dry pixels under the 19 GHz horizontal channel of the SSM/I data

152 For better generalizability, the algorithm for melt detection is chosen as the one proposed
 153 by Zwally and Fiegles (1994) rather than the sophisticated edge detection methods such as Liu et
 154 al. (2005). In Zwally and Fiegles (1994), a local mean T_b plus 30 degrees (noted as ZF+30) was
 155 used as the melt detection threshold for each pixel. This algorithm takes the spatial variation of
 156 dry snow emissivity into consideration and allows the threshold values to be adaptive to the local
 157 conditions. Figure 2 compared the time series of a wet pixel (pixel that experienced melt in the
 158 year) and a dry pixel (pixel that did not melt in the year), along with the Zwally and Fiegles
 159 threshold (ZF+30) lines for melt detection in both time series. Thus, the melt detection algorithm
 160 assigned 73 melting days to the wet pixel and 0 melting day to the dry pixel. The melt index (*MI*)
 161 of the wet pixel at the 25 km cell size, as a variable used for multi-year trend analysis of surface
 162 melt, is then computed as: $73 \text{ day} \times 625 \text{ km}^2 = 45,625 \text{ day} \cdot \text{km}^2$.

163
 164

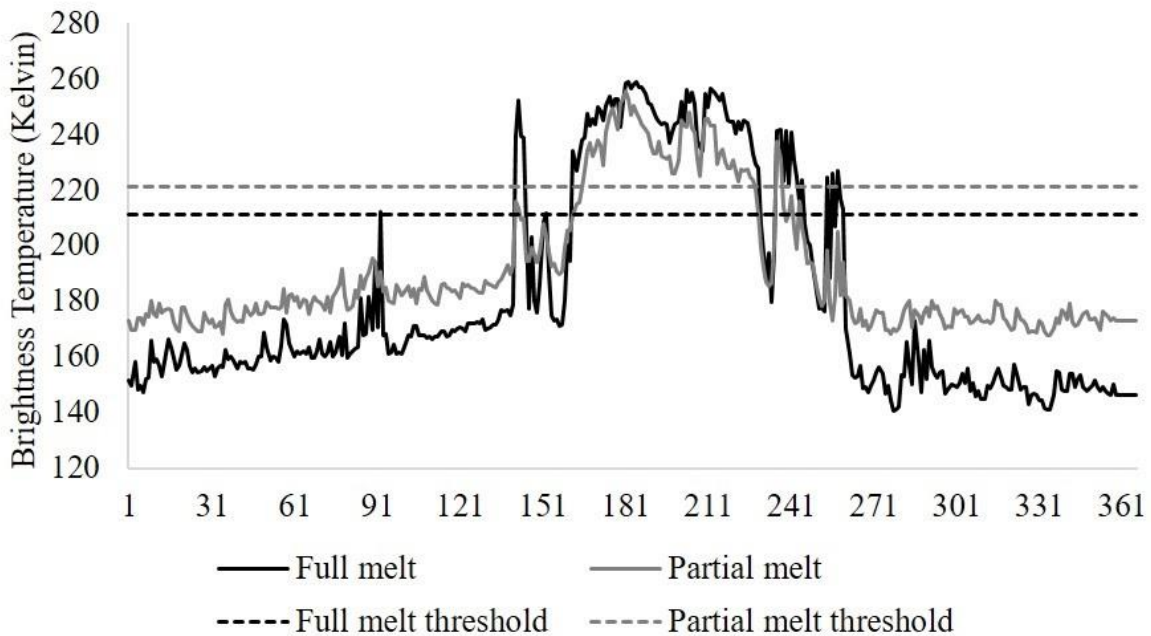


Figure 3: The annual variations of brightness temperature for typical full melt and partial melt pixels under the 19 GHz horizontal channel of the SSM/I data.

165 3.2. Least squares mixture analysis of partial melt data

166 Figure 3 illustrates a full melt pixel and a partial melt pixel and their melt detection thresholds.
 167 The melt index for the full melt pixel is $55,625 \text{ day}\cdot\text{km}^2$, and the partial melt pixel is $40,000$
 168 $\text{day}\cdot\text{km}^2$. The partial melt pixel had a similar threshold value as the full melt pixel according to
 169 Zwally and Fiegles (1994). However, because the pixel is a mix of melt and none-melt
 170 subregions within the pixel, the brightness temperature at the melt status did not rise higher than
 171 the threshold. The dilemma arises for melt days calculation: do we need to decrease the threshold
 172 to assign higher *MI* for the partial melt pixel or decrease the *MI*? From the time series view, it
 173 seems the melt duration was underestimated in the illustrated partial melt pixel. To correct the
 174 problem of underestimation, a lower threshold should be proposed, which requires the
 175 knowledge of each partial melt pixel. Even if the new threshold was assigned, in the spatial point
 176 of view, the Boolean assignment of melt overestimates the melt index because only a fraction of
 177 the 25 km by 25 km pixel actually experienced melting.

178 In figure 3, the full melt pixel and the partial melt pixel have similar shapes of their time
 179 series plots, indicating the synchronization of the two pixels in melting occurrence due to their
 180 closeness in distance. The difference of the wet snow brightness temperature in these two plots is
 181 presumed to be related to the signal mixture phenomenon. Explicitly, the wet snow brightness
 182 temperature of a partial melting pixel in a time series $T_{p,t}$ is a linear combination of the brightness
 183 temperature of melting part $T_{m,t}$ and non-melting component $T_{n,t}$ for $t = 1, 2, 3, \dots, 365$ (or 366 in a
 184 leap year), as expressed by equation 2:

$$185 \quad T_{p,t} = \alpha_m T_{m,t} + \alpha_n T_{n,t} + \varepsilon \quad (2)$$

186 where α_m is the fraction of the melting area; α_n is the fraction of the non-melting area; ϵ is the
 187 error term. The least-square solution, which minimizes the error term, under the constraints of
 188 unity and positiveness (Chein-I Chang et al., 2004), was used to solve the equation. Once the
 189 melt fraction is calculated, the melt area can be updated by multiplying the total area of an SSM/I
 190 pixel and the fraction number. For example, if a pixel is 50% melt, the total melt area from that
 191 pixel is $25 \text{ km} \times 25 \text{ km} \times 50\% = 312.5 \text{ km}^2$ instead of 625 km^2 .

192 3.3. Endmember selection

193 In equation 2, endmembers of melt and non-melt time series should be provided to obtain the
 194 solution of melt and non-melt fraction for each partial melt pixel. Endmembers are defined as
 195 pure pixels, which represent the information of a homogenous phenomenon such as melting or
 196 non-melting. $T_{n,t}$ is the time series of a non-melt pixel in a year. $T_{m,t}$ is the time series of a full
 197 melt pixel. It is relatively easy to find the non-melt pixels by using the ZF+30 criterion.
 198 However, as shown in figure 3, both the full melt and partial melt pixels were over the line of the
 199 ZF+30 criterion. Therefore, the ZF+30 criterion cannot separate full melt and partial melt pixels.
 200 However, as can be observed from figure 3, the melt edges of the full melt pixel is greater than
 201 those of the partial melt pixel because the mixture of melt and non-melt signal tends to reduce
 202 the magnitude of these edges.

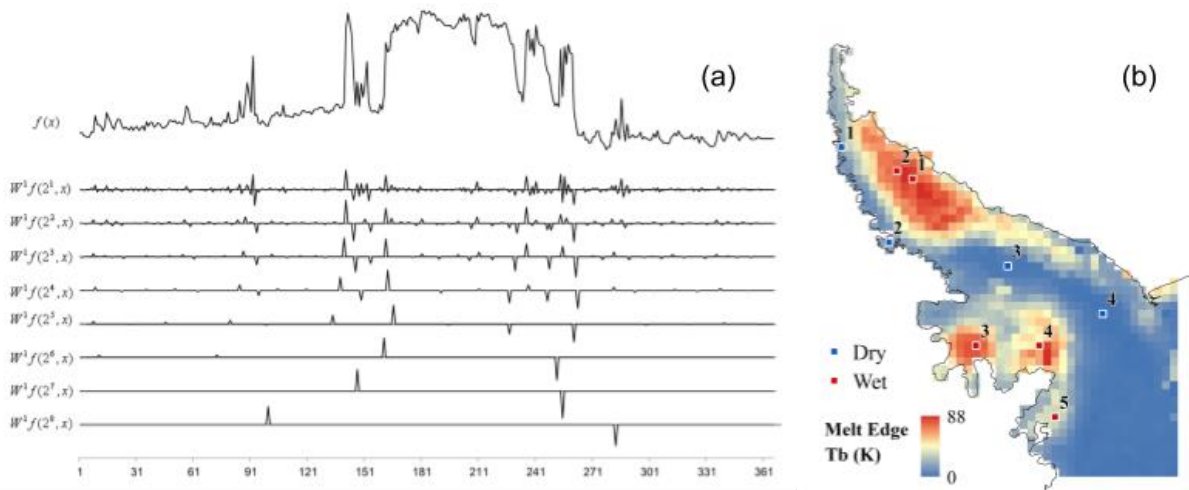


Figure 4: (a) The original daily time series of endmember wet #3 and its wavelet transformation local maxima (Liu et al., 2005) at all scales. Particularly, $W^4 f(2^4, x)$ at the fourth scale was used to classify the edges to large (GL) and small (GS) groups. (b) Locations and labels of the five full melt endmembers and four non-melt endmembers and their mean GL edge strength map. The full melt endmembers were selected from the locations with high GL strengths and the non-melt endmembers were selected from the low GL strength areas.

203 It is not difficult to run a wavelet decomposition and use a bimodal classification method
 204 to differentiate melt edges from non-melt edges at the fourth wavelet scale (Liu et al., 2005).
 205 Figure 4 (a) shows the time series of wet endmember #3 (figure 4b) and its wavelet
 206 transformation local maxima used to track melt occurrences (Liu et al., 2005). The wavelet
 207 transformation filtered the noise component and preserved stronger edges at higher scales as

208 indicators of melt events. The bimodal classification sorts the edges by their magnitude and
209 groups them to two classes - large (GL) and small (GS). The goal is to minimize the in-group
210 variance and maximize the between-group variance (Liu et al., 2005). For a wet pixel, GL
211 contains the edges caused by melt signals, while GS contains the edges caused by temperature
212 fluctuations. For non-melt pixels, both groups are non-melt edges, which are low in magnitude.
213 Therefore, the mean magnitude of the GL of a non-melt pixel is much lower than that of melt
214 pixels. The mean magnitude of the GL was used as an indicator of pixel purity: the larger the
215 mean GL edge magnitude, the more likely the pixel to be a pure melt pixel. Figure 4 (b) shows
216 the GL edge magnitude map in the study area and the locations of wet and dry endmembers.
217 Indeed, all the red-colored pixels could be considered as areas of full melt. We picked the most
218 representative ones as endmembers. The blue-colored area contains non-melt (dry) endmembers.
219 Yellow colors represent mixed pixels. We selected these endmembers to run the least squares
220 mixture analysis for melt fraction calculation within each 25-km SSM/I pixel. Melt edges are
221 clearly much stronger than non-melt edges, not only in the magnitude but also in the temporal
222 continuity. The endmembers are defined locally because the shape of the time series brightness
223 temperature changes from region to region. Each melt event is bounded by a certain terrain
224 boundary such as ridges of high mountains on ice sheets. On the other hand, the melt events on
225 ice shelves could extend far because of the flat topography. For each mixed pixel, the wet and
226 dry endmembers were picked from a tessellation of voronoi polygons defined by the locations of
227 endmembers (figure 5). Each voronoi polygon defines the nearest neighbor area to the
228 endmember candidates. Mixed pixels located within the polygon defined by an endmember will
229 be unmixed from it. The tessellation map of figure 5(a) is for wet endmember selection. The
230 tessellation map of figure 5(b) is for dry endmember selection. The nearest neighbor zones
231 assign one wet endmember based on figure 5(a) and one dry endmember based on figure 5(b) to
232 the partial melting pixels. With the wet and dry endmembers, the fraction of the melt and non-
233 melt area in each partial melting pixel were computed using equation 2.

234 **3.4. Accuracy Assessment**

235 To verify the unmixing model, we employed the high resolution product of passive microwave
236 earth system data record (PMESDR) program. The product was created by fusing multiple
237 passive microwave observations from overlapping orbits of the same sensor and/or different
238 sensors to reconstruct the super-resolution brightness temperature data. In terms of the spatial
239 resolution, this product is comparable to another high resolution product from the QUIKSCAT
240 satellite SeaWinds Ku band radar image using a similar high-resolution reconstruction algorithm.
241 In fact, the super-resolution QUIKSCAT product was used for accuracy assessment in many
242 snow melt mapping projects (Bhattacharya et al., 2009; De Freitas et al., 2018). However, the
243 problem of QUIKSCAT data is its short life. It collected global images from 1999 to 2009 for
244 about ten years, which already exceeded its designed life. The PMESDR program created super-
245 resolution passive microwave images spanning much longer time than QUIKSCAT, and because
246 it is a product of radiometers rather than scatterometers, it is superior to QUIKSCAT images for
247 verifying the unmixing algorithm on passive microwave images.

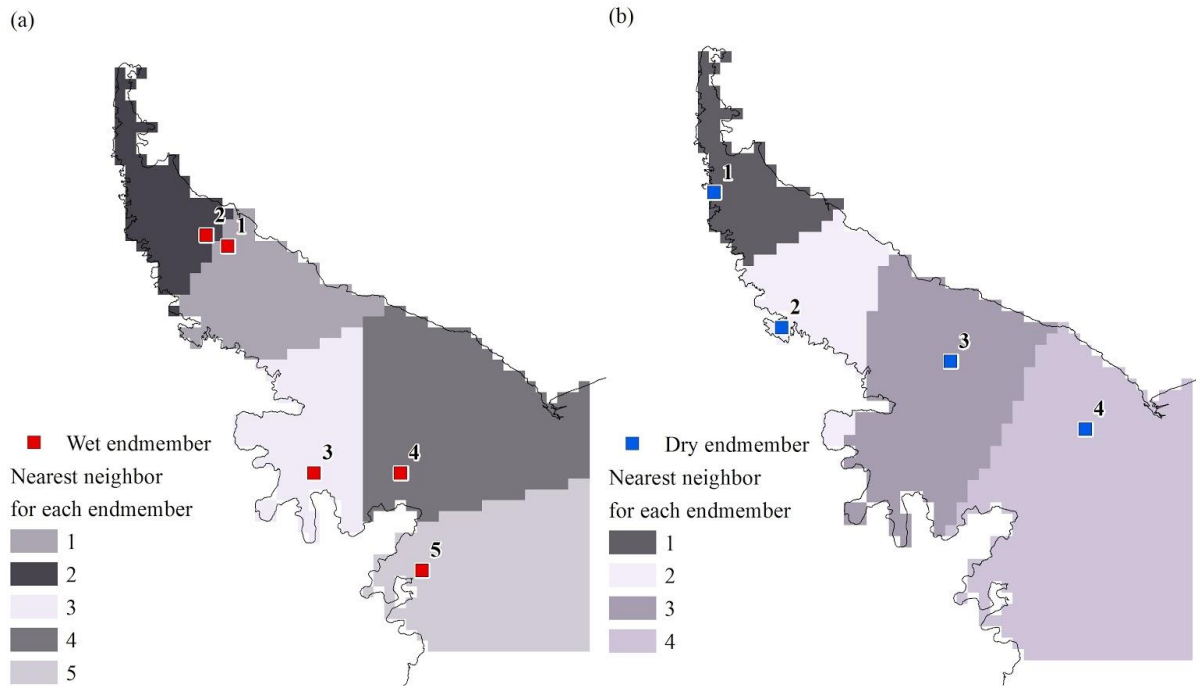


Figure 5: Spatially constrained endmember selection defined by voronoi polygons

248 The comparison between the model output and the high resolution data used the melt
 249 index (MI) variable derived from the time series of passive microwave data. Melt index (in
 250 $\text{day}\cdot\text{km}^2$) is the sum of the daily melt extents for a certain area (e.g. the entire Antarctica or the
 251 Antarctic Peninsula) for the entire season (Liu et al., 2006). Melt index is a convenient variable
 252 to study the interannual trends of surface melt in Antarctica and Greenland and an indicator for
 253 climate change (Bhattacharya et al., 2009; Liu et al., 2006; Oza, 2015; Tedesco, 2009). The
 254 formula of the melt index is:

$$MI = \sum_{i=1}^n md_i \cdot A \quad (3)$$

256 where A is the area size of one pixel (assuming it is a constant for all pixels), N is the total
 257 number of pixels, and md_i is the number of melt days (melting duration) within a year for the
 258 pixel i . Each $25 \text{ km} \times 25 \text{ km}$ SSM/I pixel contains 16 high resolution PMESDR pixels (6.25 km
 259 $\times 6.25 \text{ km}$). The total MI of the 16 PMESDR pixels was compared to the unmixed SSM/I pixel
 260 MI . The sum of MI for the entire study area as well as the root mean square error (RMSE) from
 261 pixel-wise comparison of all the land pixels were reported in table 1.

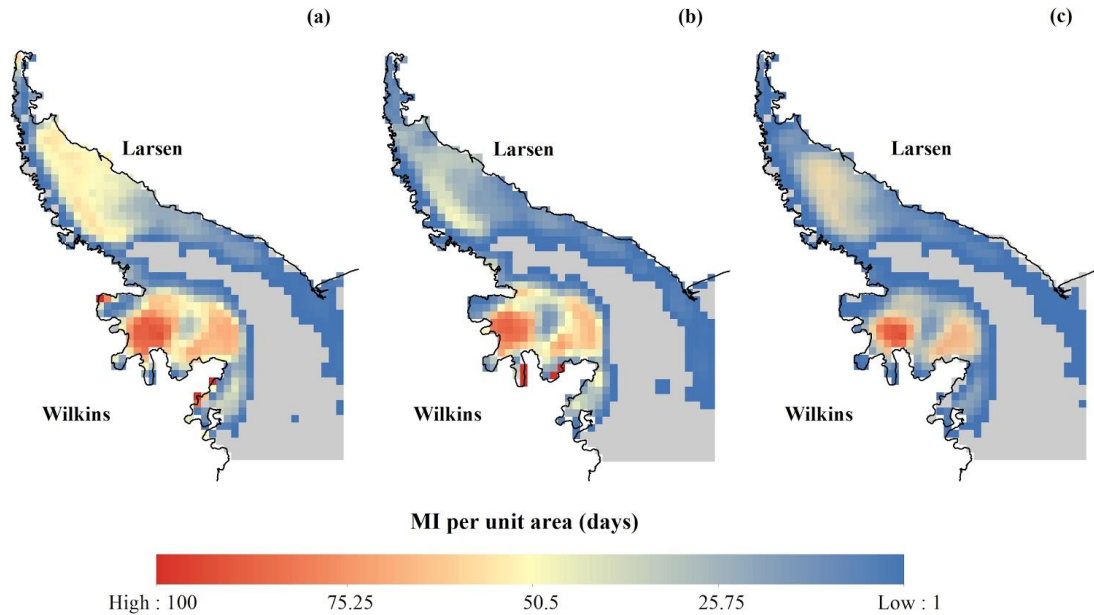
262 **4. Results and discussions**263 **4.1. Linear mixture analysis and accuracy assessment**

Figure 6: Comparing *MI* of (a) original SSM/I, (b) PMESDR, and (c) LSMA result.

264 Table 1 summarizes the total melt index of the Antarctic Peninsula and pixel-wise statistical
 265 values calculated from the three datasets: (1) original SSM/I (2) unmixed SSM/I from LSMA,
 266 and (3) high-resolution PMESDR images. The total melt index of the entire study area in the
 267 Austral summer of 2012-13 differed from each other. The melt index calculated from the original
 268 SSM/I data is about 50% larger than that from PMESDR, showing that there was a significant
 269 bias of overestimation of the reported surface melt using the original SSM/I data. The *MI* of the
 270 least squares mixture analysis (LSMA) was 43% smaller than the original SSM/I data and
 271 slightly (14%) smaller than the PMESDR result.

272 Table 1: Comparison of *MI* from different datasets and their RMSE referenced to PMESDR data.

Melt index (10^6 day·km ²)	SSM/I	LSMA	PMESDR
Study area total	11.365	6.478	7.565
RMSE	0.0104	0.0083	N/A

273 The lower RMSE of the LSMA result indicates that the subpixel melt index improved the
 274 confidence and accuracy over the Boolean calculation of melt index from SSM/I images. The
 275 14% lower *MI* of the unmixed SSM/I data is also justifiable, because later in the discussion 4.4
 276 we will show the LSMA result from the PMESDR images, which was further lower than the

277 Boolean calculation from PMESDR data. In other words, overestimation also exists in the high
 278 resolution PMESDR images. Therefore, the 14% lower MI from the LSMA of SSM/I images
 279 was actually correct. Though, the LSMA calculation of melt index was satisfactory given the
 280 large bias of the Boolean calculation products. Figure 6 shows the maps of the original SSM/I MI
 281 (figure 6a), PMESDR MI (figure 6b), and the MI by unmixing calculation (figure 6c) for each
 282 land pixel. Compared with the high resolution PMESDR MI map (figure 6b), the overestimation
 283 of the SSM/I MI (figure 6a) mainly occurred on the Larsen Ice Shelf and the coast of Wilkins.
 284 The unmixing result (figure 6c) had overestimation on the Larsen Ice Shelf but underestimation
 285 on the Wilkins Ice Shelf. The overall pattern of the LSMA MI map matches the PMESDR MI
 286 map better, indicating a better accuracy of the estimated melt index from the unmixing method.

287 **4.2. Impact of pixel size and endmembers purity on least squares mixture analysis**

288 The LSMA model assumes the wet and dry pixels (figure 4b) picked from the study area are pure
 289 endmembers. However, with such a large pixel size of the 25-km SSM/I images, it would be
 290 difficult to find fully melted pixels. Therefore, we have to acknowledge that the endmembers of
 291 wet pixels could only be approximations and uncertainty could be brought to the LSMA model
 292 by the impurity of endmembers. Strictly, we may not be able to find real pure endmembers to
 293 implement the unmixing method at such a scale as satellite radiometer mapping. It is interesting
 294 to test, however, if some relaxation on the pure endmember selection criterion is acceptable and
 295 if the LSMA model can be improved by using the endmembers derived from the high resolution
 296 product rather than from the same SSM/I scene.

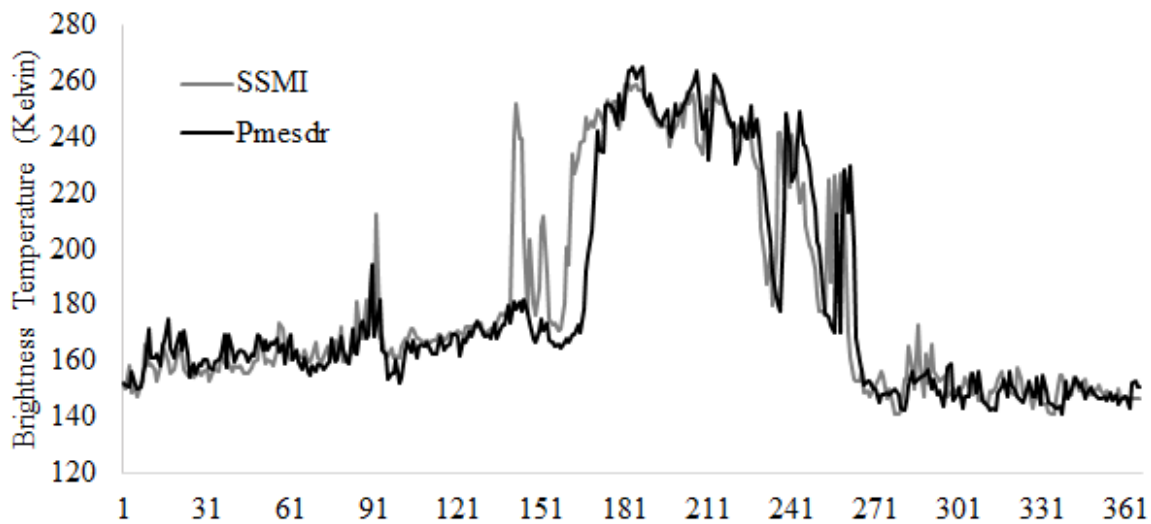


Figure 7: The comparison between the PMESDR pixel and the SSM/I pixel as endmembers.

297 Theoretically, the high resolution images should contain more pure pixels for the unmixing
 298 algorithm to use. To test how much the impurity of endmembers had impacted the unmixing
 299 results, we chose endmembers from the high resolution PMESDR images to implement the
 300 LSMA unmixing calculation. The PMESDR pixels were picked up from the center location of
 301 the SSM/I endmember pixels. As shown in figure 7, the PMESDR endmember has slightly
 302 higher brightness temperature values during the melting time. Then, the unmixing of the SSM/I
 303

304 image was performed using the endmembers that were supposed to be more “pure” because the
 305 resolution of the PMESDR pixels was better. However, the unmixing results showed the RMSE
 306 of unmixing the SSM/I images using the PMESDR endmembers was 0.0088 ($10^6 \text{ day}\cdot\text{km}^2$),
 307 which was very close to but 6.02% higher than that using the SSM/I endmembers. Therefore,
 308 although the endmember impurity could cause uncertainty for unmixing, the endmembers
 309 obtained from the high resolution image did not improve the LSMA model. On the other hand,
 310 the high similarity between the unmixing results from SSM/I endmembers and the PMESDR
 311 endmembers indicates that the pixel resolution and impurity of endmembers did not bring much
 312 uncertainty to the LSMA model.

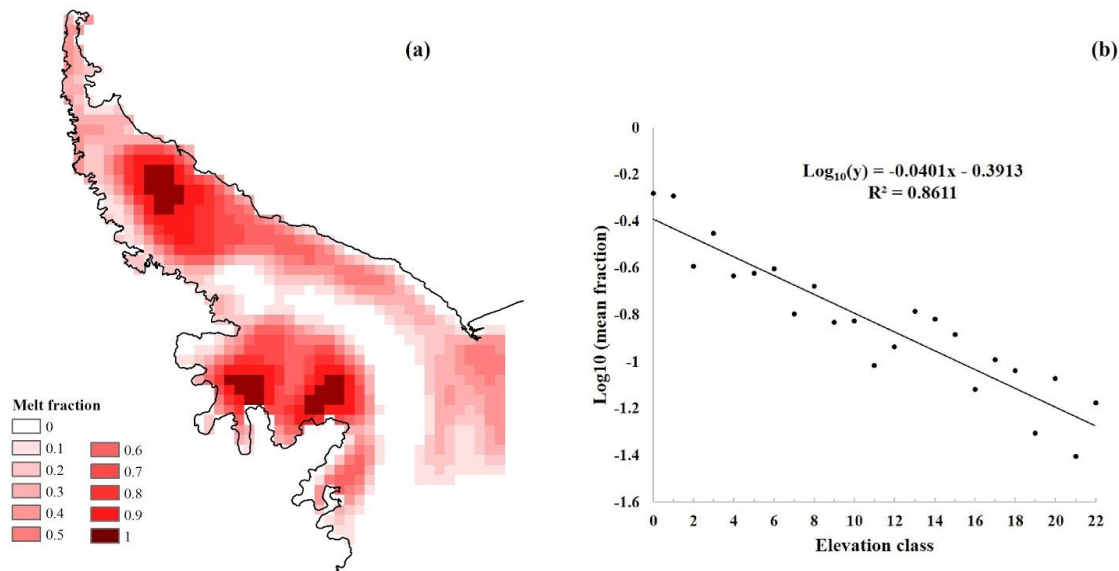


Figure 8: (a) The melt fraction map calculated from LSMA and (b) the scatterplot of between the melt fraction and mean elevation of the pixel.

313 **4.3. Relationship with elevation**

314 The spatial pattern of the melt fraction map in figure 8(a) shows a high resemblance with the
 315 topographic maps published for the Antarctic Peninsula. Therefore, we suspect the elevation may
 316 play an important role in the partial melting problem. We obtained a 1-km elevation model of
 317 Antarctica (Bamber et al., 2009) to analyze its correlation with the melt fraction map. In the
 318 scatterplot (figure 8b), each elevation class is defined by a 100-m interval from the lowest to the
 319 highest and named by the integer number rounded up from the 100th of their elevation values. In
 320 each elevation class, the mean melt fraction was calculated to make the scatterplot with the
 321 elevation class. Because of the non-linearity of the original scatterplot, a logarithm was taken on
 322 the mean melt fraction values. The melt fraction is almost 100% on the ice shelves near the coast
 323 and goes down sharply with the increasing elevation towards the mountains. The scatterplot
 324 shows a clear inverse log-linear trend ($p < 0.0001$) between the elevation class and the mean melt
 325 fraction. It suggests that, in the study area, the partial melting problem on the ice sheets is mainly
 326 caused by the elevation change. The logarithm relationship between elevation and melt fraction

327 indicates that the elevation has little impact on melt fraction over low-lying and flat ice shelves
 328 and, when the elevation is getting higher (e.g., 1000 m), it becomes a dominant variable to
 329 control partial melt fractions.

330 **4.4. Unmixing the high resolution PMESDR images**

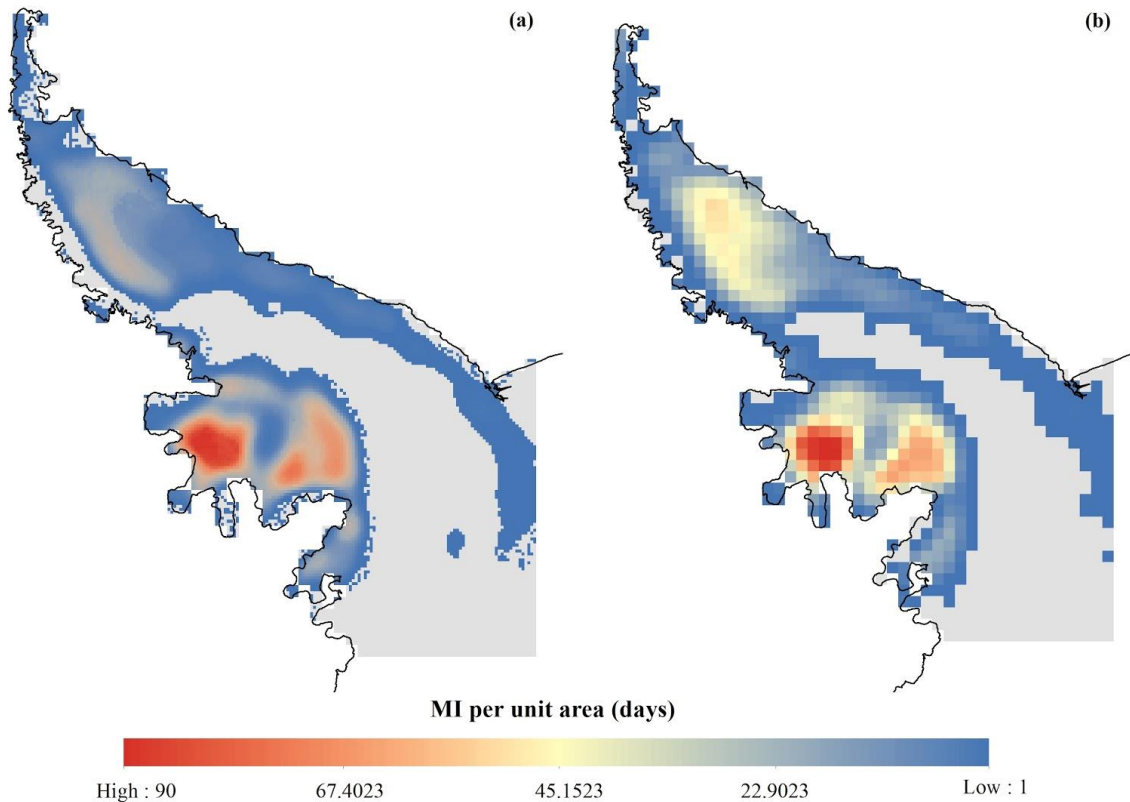


Figure 9: Subpixel melt index map from (a) PMESDR images and (b) original SSM/I images.

331 From the above discussions, we have proved the ability of LSMA to correct the bias introduced
 332 by the Boolean calculation of melt index. It is interesting to test how much difference is in the
 333 melt index derived from high resolution PMESDR images if the Boolean calculation was
 334 replaced by the LSMA model. The purpose of the test is to validate the application of LSMA to
 335 higher resolution image products. Therefore, we applied the same approach to the high resolution
 336 PMESDR images and compared the unmixed *MI* with that from the SSM/I images.

337 Figure 9a shows the melt index map from the LSMA calculation of PMESDR images
 338 using the spatially constrained endmembers. Compared to the unmixed melt index map from the
 339 original SSM/I images (figure 9b), the resolution and spatial details look much better. The melt
 340 index from the least squares mixture analysis for the whole study area was $4.417 (10^6 \text{ day} \cdot \text{km}^2)$,
 341 which is about 41.6% lower than the Boolean calculation *MI* from PMESDR. This difference is
 342 consistent with the comparison between the Boolean *MI* and unmixed *MI* from SSM/I images,

343 where the unmixed product was 43% lower. The overestimation bias of the Boolean calculation
344 was therefore corrected by the LSMA method. We used the high resolution product of PMESDR
345 images as a reference and confirmed such treatment improved the accuracy of the melt index
346 estimation. Although owing to the unavailability of a higher resolution product than PMESDR
347 data to verify its LSMA result, we can reasonably infer that the unmixed PMESDR melt index is
348 the best map product for surface melt.

349 **5. Conclusions**

350 The large pixel size of passive microwave images has caused large uncertainty for monitoring
351 surface melt over Antarctic Ice Margins. The melt maps need to be updated using high resolution
352 data to reduce uncertainty. This paper proposes a least squares mixture analysis (LSMA) of the
353 brightness temperature time series to calculate the subpixel melt index that is comparable with
354 the high resolution products. We found that the map of Boolean surface melt derived from the
355 SSM/I images could overestimate surface melt by 50% in Larsen and Wilkins Ice Shelves. With
356 the treatment of LSMA, the overestimation of surface melt was offset and the uncertainty was
357 also reduced.

358 The second finding from our analysis was that the unmixing method would reduce the *MI*
359 estimate by a certain amount (e.g., 40-45% in our study area) regardless of the resolution of the
360 image used. As the partial melting problem has caused overestimation of *MI*, the reduction of *MI*
361 from the unmixing analysis was correct and necessary. Therefore, we recommend such an
362 unmixing approach to be always applied to surface melt calculation from satellite radiometer
363 data.

364 The third finding is that the melt fraction is inversely related to the elevation at a log-
365 linear form. The log-linear regression equation between melt fraction and elevation suggests that
366 the partial melting phenomenon in our study area could be largely controlled by topography on
367 the high-elevation ice sheets. Therefore, partial melting of the passive microwave image pixels
368 could be a severe problem for melt occurred near the Antarctic ice shelf grounding lines.

369 To illustrate and verify the time series unmixing method, we focused on the study area of
370 the Antarctic Peninsula. With the evidence collected from this area, we will be able to generalize
371 the application of the spatially constrained least squares mixture analysis to other major ice
372 shelves of Antarctica and refine the trend analysis of Antarctic surface melt with higher
373 confidence and less uncertainty.

374 **Acknowledgments, Samples, and Data**

375 This work was supported by the 2019 Manship Summer Research Fellowship of the College of
376 Humanities and Social Sciences at Louisiana State University. The authors claim no real or
377 perceived financial conflicts of interests. All datasets used in this research were obtained from
378 the National Snow and Ice Data Center (NSIDC).

379
380

381 **References**

- 382 Abdalati, W., & Steffen, K. (1995). Passive microwave-derived snow melt regions on the
383 Greenland Ice Sheet. *Geophysical Research Letters*, 22(7), 787–790.
- 384 Abdalati, W., & Steffen, K. (1997). Snowmelt on the Greenland Ice Sheet as Derived from
385 Passive Microwave Satellite Data. *Journal of Climate*, 10(2), 165–175.
- 386 Abdalati, W., & Steffen, K. (2001). Greenland ice sheet melt extent: 1979–1999. *Journal of*
387 *Geophysical Research, D: Atmospheres*, 106(D24), 33983–33988.
- 388 Armstrong, R., Knowles, K., Brodzik, M. J., & Hardman, M. A. (1994). DMSP SSM/I-SSMIS
389 Pathfinder Daily EASE-Grid Brightness Temperatures, Version 2, Southern Hemisphere
390 [Data set]. <https://doi.org/10.5067/3EX2U1DV3434>
- 391 Bamber, J. L., Gomez-Dans, J. L., & Griggs, J. A. (2009). A new 1 km digital elevation model of
392 the Antarctic derived from combined satellite radar and laser data – Part 1: Data and
393 methods. *The Cryosphere*. <https://doi.org/10.5194/tc-3-101-2009>
- 394 Bhattacharya, I., Jezek, K. C., Wang, L., & Liu, H. (2009). Surface melt area variability of the
395 Greenland ice sheet: 1979–2008. *Geophysical Research Letters*, 36(20), 165.
- 396 Brodzik, M. J., & Long, D. G. (2015). Calibrated Passive Microwave Daily EASE-Grid 2.0
397 Brightness Temperature ESDR (CETB): Algorithm Theoretical Basis Document.
398 *MEaSURES Project White Paper*.
- 399 Brodzik, M. J., Long, D. G., Hardman, M. A., Paget, A., & Armstrong, R. (2018). MEaSURES
400 Calibrated Enhanced-Resolution Passive Microwave Daily EASE-Grid 2.0 Brightness
401 Temperature ESDR, Version 1 [Data set].
402 <https://doi.org/10.5067/MEASURES/CRYOSPHERE/NSIDC-0630.001>
- 403 van den Broeke, M. (2005). Strong surface melting preceded collapse of Antarctic Peninsula ice
404 shelf. *Geophysical Research Letters*, 32(12). Retrieved from
405 <https://agupubs.onlinelibrary.wiley.com/doi/abs/10.1029/2005GL023247>
- 406 Chein-I Chang, Hsuan Ren, Chein-Chi Chang, D’Amico, F., & Jensen, J. O. (2004). Estimation
407 of subpixel target size for remotely sensed imagery. *IEEE Transactions on Geoscience and*
408 *Remote Sensing: A Publication of the IEEE Geoscience and Remote Sensing Society*, 42(6),
409 1309–1320.
- 410 De Freitas, M. W. D., Mendes Júnior, C. W., Arigony-Neto, J., Costi, J., & Simões, J. C. (2018).
411 A multiscale subpixel mixture analysis applied for melt detection using passive microwave
412 and radar scatterometer image time series of the Antarctic Peninsula (1999–2009). *Annals*
413 *of Glaciology*, 59(76pt1), 16–28.
- 414 Doake, C. S. M., & Vaughan, D. G. (1991). Rapid disintegration of the Wordie Ice Shelf in
415 response to atmospheric warming. *Nature*, 350(6316), 328–330.
- 416 Fahnestock, M. A., Abdalati, W., & Shuman, C. A. (2002). Long melt seasons on ice shelves of
417 the Antarctic Peninsula: an analysis using satellite-based microwave emission
418 measurements. *Annals of Glaciology*, 34, 127–133.
- 419 Gilbert, R., & Domack, E. W. (2003). Sedimentary record of disintegrating ice shelves in a
420 warming climate, Antarctic Peninsula. *Geochemistry, Geophysics, Geosystems*, 4(4), 206.
- 421 Gолledge, N. R., Keller, E. D., Gomez, N., Naughten, K. A., Bernalles, J., Trusel, L. D., &
422 Edwards, T. L. (2019). Global environmental consequences of twenty-first-century ice-
423 sheet melt. *Nature*, 566(7742), 65–72.
- 424 Holland, P. (2010). Warm bath for an ice sheet. *Nature Geoscience*, 3(3), 147–148.

- 425 Liang, L., Li, X., & Zheng, F. (2019). Spatio-Temporal Analysis of Ice Sheet Snowmelt in
426 Antarctica and Greenland Using Microwave Radiometer Data. *Remote Sensing*, *11*(16),
427 1838.
- 428 Liu, H., Wang, L., & Jezek, K. C. (2005). Wavelet-transform based edge detection approach to
429 derivation of snowmelt onset, end and duration from satellite passive microwave
430 measurements. *International Journal of Remote Sensing*, *26*(21), 4639–4660.
- 431 Liu, H., Wang, L., & Jezek, K. C. (2006). Spatiotemporal variations of snowmelt in Antarctica
432 derived from satellite scanning multichannel microwave radiometer and Special Sensor
433 Microwave Imager data (1978–2004). *Journal of Geophysical Research*, *111*(F1), 787.
- 434 Long, D. G., & Brodzik, M. J. (2016). Optimum Image Formation for Spaceborne Microwave
435 Radiometer Products. *IEEE Transactions on Geoscience and Remote Sensing: A
436 Publication of the IEEE Geoscience and Remote Sensing Society*, *54*(5), 2763–2779.
- 437 Long, D. G., & Daum, D. L. (1998). Spatial resolution enhancement of SSM/I data. *IEEE
438 Transactions on Geoscience and Remote Sensing: A Publication of the IEEE Geoscience
439 and Remote Sensing Society*, *36*(2), 407–417.
- 440 MacAyeal, D. R., Scambos, T. A., Hulbe, C. L., & Fahnestock, M. A. (2003). Catastrophic
441 ice-shelf break-up by an ice-shelf-fragment-capsize mechanism. *Journal of Glaciology*,
442 *49*(164), 22–36.
- 443 Mote, T. L., & Anderson, M. R. (1995). Variations in snowpack melt on the Greenland ice sheet
444 based on passive-microwave measurements. *Journal of Glaciology*, *41*(137), 51–60.
- 445 Mote, T. L., Anderson, M. R., Kuivinen, K. C., & Rowe, C. M. (1993). Passive microwave-
446 derived spatial and temporal variations of summer melt on the Greenland ice sheet. *Annals
447 of Glaciology*, *17*, 233–238.
- 448 NOAA. (2019, October 15). NOAA/NGDC - Earth Observation Group - Defense Meteorological
449 Satellite Program, Boulder. Retrieved March 21, 2020, from
450 <https://ngdc.noaa.gov/eog/sensors/ssmi.html>
- 451 Oza, S. R. (2015). Spatial–temporal patterns of surface melting observed over Antarctic ice
452 shelves using scatterometer data. *Antarctic Science / Blackwell Scientific Publications*,
453 *27*(4), 403–410.
- 454 Ridley, J. (1993). Surface melting on Antarctic Peninsula ice shelves detected by passive
455 microwave sensors. *Geophysical Research Letters*, *20*(23), 2639–2642.
- 456 Scambos, T. A., Hulbe, C., Fahnestock, M., & Bohlander, J. (2000). The link between climate
457 warming and break-up of ice shelves in the Antarctic Peninsula. *Journal of Glaciology*,
458 *46*(154), 516–530.
- 459 Steffen, K. (1995). Surface energy exchange at the equilibrium line on the Greenland ice sheet
460 during onset of melt. *Annals of Glaciology*, *21*, 13–18.
- 461 Steig, E. J., Schneider, D. P., Rutherford, S. D., Mann, M. E., Comiso, J. C., & Shindell, D. T.
462 (2009). Warming of the Antarctic ice-sheet surface since the 1957 International
463 Geophysical Year. *Nature*, *457*(7228), 459–462.
- 464 Tedesco, M. (2009). Assessment and development of snowmelt retrieval algorithms over
465 Antarctica from K-band spaceborne brightness temperature (1979–2008). *Remote Sensing
466 of Environment*, *113*(5), 979–997.
- 467 Torinesi, O., Fily, M., & Genthon, C. (2003). Variability and Trends of the Summer Melt Period
468 of Antarctic Ice Margins since 1980 from Microwave Sensors. *Journal of Climate*, *16*(7),
469 1047–1060.

- 470 Vaughan, D. G., & Doake, C. S. M. (1996). Recent atmospheric warming and retreat of ice
471 shelves on the Antarctic Peninsula. *Nature*, 379(6563), 328–331.
- 472 Wang, L., & Liu, H. (2017). Seasonal melt extent and duration [in “State of the Climate in
473 2016”]. *Bulletin of the American Meteorological Society*, 98(8), S162–S163.
- 474 Zwally, H. J. (2002). Surface Melt-Induced Acceleration of Greenland Ice-Sheet Flow. *Science*.
475 <https://doi.org/10.1126/science.1072708>
- 476 Zwally, H. J., & Fiegles, S. (1994). Extent and duration of Antarctic surface melting. *Journal of*
477 *Glaciology*, 40(136), 463–475.
- 478 Zwally, H. J., & Gloersen, P. (1977). Passive microwave images of the polar regions and
479 research applications. *The Polar Record*, 18(116), 431–450.